Acta Astronautica 127 (2016) 634–643

Contents lists available at ScienceDirect

Acta Astronautica

journal homepage: www.elsevier.com/locate/aa

Computational investigation on combustion instabilities in a rocket combustor

Lei Yuan [a,b], Chibing Shen [a,b,*]

[a] Science and Technology on Scramjet Laboratory, National University of Defense Technology, Changsha 410073, China
[b] College of Aerospace Science and Engineering, National University of Defense Technology, Changsha 410073, China

ARTICLE INFO

Article history:
Received 27 August 2015
Accepted 5 June 2016
Available online 9 July 2016

Keywords:
Combustion instability
Numerical simulation
Velocity ratio

ABSTRACT

High frequency combustion instability is viewed as the most challenging task in the development of Liquid Rocket Engines. In this article, results of attempts to capture the self-excited high frequency combustion instability in a rocket combustor are shown. The presence of combustion instability was demonstrated using point measurements, along with Fast Fourier Transform analysis and instantaneous flowfield contours. A baseline case demonstrates a similar wall heat flux profile as the associated experimental case. The acoustic oscillation modes and corresponding frequencies predicted by current simulations are almost the same as the results obtained from classic acoustic analysis. Pressure wave moving back and forth across the combustor was also observed. Then this baseline case was compared against different fuel-oxidizer velocity ratios. It predicts a general trend: the smaller velocity ratio produces larger oscillation amplitudes than the larger one. A possible explanation for the trend was given using the computational results.

1. Introduction

High frequency combustion instability is considered as a major challenge in the development of the Liquid Rocket Engines (LRE). It is very sensitive to the operation parameter, because the process of feeding little energy into the acoustic mode will lead to high frequency combustion instability. When it occurs, the pressure fluctuates, which can introduce large thermal and mechanical stresses in the combustor, resulting in decreased performance, unacceptable vibrations or even engine failure [1–3]. At present, our understanding of combustion instability in LRE is limited and predicting these combustion instabilities is strongly requested.

The fundamental mechanisms leading to high frequency combustion instability in LRE are the coupling between the sub-processes and the acoustic oscillation in combustor, such as injection, atomization, vaporization, mixing and chemical reactions. To date various complex levels of computational models have been employed to deal with high frequency combustion instability. The basic engineering level models based upon wave equations and transfer functions have been used to predict the relative growth rates of acoustic modes. These models can be used to study rapidly effect of parameters on the combustion instability, but are limited in exploring flow detail [4]. Furthermore, the transfer functions need to be appropriately designed and calibrated with the use of high quality instability data. CFD method is regarded as an effective tackles to investigate combustion instability, because it can obtain the detailed flow field parameters and it does not necessarily require transfer functions to represent the dynamic response. The potential mechanism for sustaining high frequency combustion instability may be the coupling between the unsteady motion and the heat release [5–8]. Consequently, in order to investigate high frequency combustion instability, it is crucial to capture the unsteady motion in the combustor. The most detailed computational models use Large Eddy Simulation (LES) or Direct Numerical Simulation (DNS) to calculate the unsteady, reacting, turbulent flow field. Though these models can be used to explore the flow detail of combustion instability, they are still in their infancy due to the enormous demands on computer resources [9–11].

In the present paper, combustion instability is investigated by a hybrid RANS/LES turbulence model featuring little demands on computer resources. Also, this method can be used to capture the flow detail in the combustor [12–14]. An important question is whether the unsteady heat release can be simulated in a realistic manner that allows self-sustained oscillations. This question is addressed by tracking the large scale mixing dynamics directly and modeling sub-grid scale events and boundary-layer details through an unsteady RANS model. Numerical simulation results are explored in detail with the objective of developing the

* Corresponding author at: Science and Technology on Scramjet Laboratory, National University of Defense Technology, Changsha 410073, China.
E-mail addresses: yuanleistone@sina.cn (L. Yuan), cbshen@nudt.edu.cn (C. Shen).

http://dx.doi.org/10.1016/j.actaastro.2016.06.015
0094-5765/

understanding of the physics involved in the unstable combustion.

This paper is structured in the following manner. First, the description of the problem and simulation configure is presented. Next, description of the computational setup and verification studies were accomplished. The final section presents the results of a number of cases and compares the predictions for different velocity ratios. Differences among the cases are highlighted by examining the filtered pressure signals, mode shapes, instantaneous vorticity field and Fast Fourier Transform (FFT) spectrum along with frequency content of the pressure signals. Finally, conclusions and future work are presented.

2. Geometrical configure and operating conditions

2.1. Geometrical configure

Simulations are carried out in the exact configuration used in the experimental investigation on the Pennsylvania State University test bench [15]. Fig. 1 shows the schematic of the engine. The engine is composed of a shear coaxial injector, cylindrical chamber and convergent–divergent nozzle. The length of the combustion chamber is 337 mm. The total length of the convergent and divergent sections of the nozzle is 51 mm (26 mm and 25 mm respectively). The combustion chamber diameter is 38.1 mm, and the throat diameter is 8.166 mm.

Fig. 2 depicts the schematic of the injector. The exit diameter of the central oxidizer stream is 5.26 mm, and the oxidizer post is recessed 0.430 mm behind the chamber face. The inner and outer diameters at the exit of the annular fuel stream are 6.3 mm and 7.5 mm, respectively.

2.2. Operation conditions

The flow conditions, including composition, key reference properties, and flow characteristics of the oxidizer and fuel streams are listed in Table 1. The mass flow rate of oxidizer stream (oxygen:0.945, water:0.055 (mass fraction)) was 0.0904 kg/s and was injected at a temperature of 711 K. The mass flow rate of fuel stream (hydrogen:0.402, water:0.598 (mass fraction)) was 0.0331 kg/s and was injected at a temperature of 800 K. The reference pressure was 5.2 MPa. At this pressure the corresponding bulk exit velocities from the injector are 154 m/s for the oxidizer stream and 764 m/s for the fuel stream. Based on the hydraulic diameter, the corresponding Reynolds numbers are 604,000 and 169,000 respectively.

3. Computational setup

3.1. Solver and models

Numerical simulations performed in this paper were carried out using the density-based solver in the commercial code ANYSYS [16]. The current simulations solve the Favre-filtered compressible multispecies and unsteady Navier–Stokes equations in conservative form ($\bar{\phi}$ denotes the Reynolds-averaged value of a variable ϕ, and $\tilde{\varphi}$ is its mass-weighted (Favre) average).

$$\frac{\partial \vec{Q}}{\partial t} + \nabla\cdot\left(\vec{F} - \vec{F}_v\right) = \vec{H} \tag{1}$$

Where $\vec{Q}$ is the vector of conservative variables, t is the physical time, $\vec{F}$ and $\vec{F}_v$ represent inviscid and viscous flux vectors, respectively. $\vec{H}$ is the source vector that includes local production or destruction. The vector of conservative variables is given by

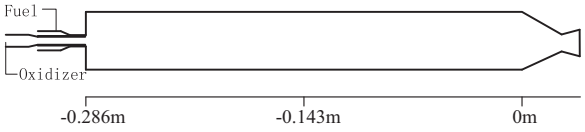

Fig. 1. Schematic of the engine.

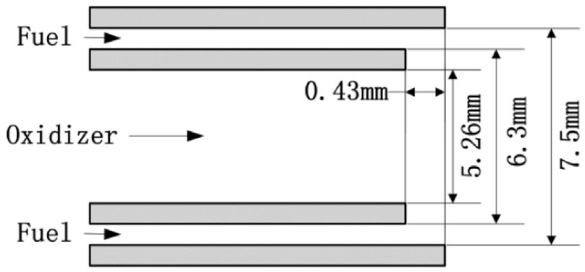

Fig. 2. Schematic of the NO. 2 injector.

Table 1
Flow conditions for inlet.

	Oxidizer	Fuel
Stream composition		
Composition by mass	0.945(O_2) 0.0550(H_2O)	0.402(H_2) 0.598(H_2O)
Total mass flow rate, kg/s	0.0904	0.0331
Reference properties		
Temperature, K	711	800
Pressure, MPa	5.2	5.2
Density, kg/m^3	28.6	3.33
Dynamic viscosity, Pa s	3.62×10^{-5}	1.81×10^{-5}
Flow Characteristics		
Bulk velocity, m/s	154	764
Reynolds number	604,000	169,000

$$Q = \left(\bar{\rho}, \bar{\rho}\tilde{u}, \bar{\rho}\tilde{v}, \bar{\rho}\tilde{h}^0 - \bar{p}, \bar{\rho}\tilde{Y}_l\right)^T \tag{2}$$

with the density, $\bar{\rho}$, flow velocities, $\tilde{u}_i$, stagnation enthalpy, $\tilde{h}_0$, pressure, $\tilde{p}$, and species mass fractions, $\tilde{Y}_l$. $l = 1, 2, \ldots, N_{SP}-1$, where N_{SP} is the number of species. The reader is referred to [17] for a thorough description of the governing equations.

Turbulence is modeled using Detached Eddy Simulation (DES) turbulence model, which functions as a sub-grid-scale model in regions where the grid density is fine enough for the LES, and as a Reynolds-averaged model in regions (essentially boundary layers) where it is not. So “LES model” is used to compute large eddy motion, while two-equation k–w model is applied to compute near wall turbulence. DES is sensitive to the grid density and can be adjusted to a lower level of eddy viscosity (relative to RANS), thus allowing a smooth transition between the different regions being modeled. The detailed description of this model can be found in publications [18,19]. Shipley et al. [20] presented that global reactions allow the coupling of pressure and unsteady heat release to be captured while minimizing the number of species that must be included. Large unsteady calculations may take several months to complete. Therefore, in the present simulations combustion process is modeled by means of a three-species, single-step, finite rate global reaction that is given as

$$H_2 + 0.5O_2 \rightarrow H_2O \tag{3}$$

The associated Arrhenius-based kinetics mechanism was used as the control mechanism of the combustion reaction, which readily incorporates the effects of pressure fluctuations on heat release, an interaction that is imperative for combustion instability modeling, since these fluctuations are ultimately responsible for

Table 2
Reaction rate parameters.

Parameter	Eq. (4)
A_r, $\frac{1}{K^{\beta_r}\cdot s}\left(\frac{kmol}{m^3}\right)^{1-a-b}$	9.87×10^8
β_r	0
E_r, J/kmol	3.1×10^7
a	1
b	1

driving instability in the configuration considered. The reaction rate is shown in Eq. (4) and its value is determined from the parameters presented in Table 2, where A_r is the pre-exponential factor, β_r is temperature exponent (dimensionless), E_r is the activation energy for the reaction, a and b are the rate exponents, and R is the universal gas constant. Discretion process of the conservation equations are accomplished by means of a second order scheme. An implicit dual-time method is used to eliminate approximate factorization errors. The scheme is second-order temporal accuracy and a physical time step of 0.05 μs is used for all simulations. Mechanisms originating from unsteady motion which can lead to fluctuations of heat release, are covered in the present computational setup.

$$\hat{R} = A_r\cdot T^{\beta_r}\cdot e^{-E_r/RT}\cdot\left(C_{H_2}\right)^a\cdot\left(C_{O_2}\right)^b \tag{4}$$

3.2. Grid generation and boundary conditions

Details of the computational grid are shown in Fig. 3. The finest resolution is located in the injector region, while the resolution is coarser in the rest of the computational domain. A series of grid sizes was computed to ensure gird independence. All results shown here are for the finest grids which were quite highly resolved (249,034 cells).

In the present simulation work, characteristic inflow with constant mass flow rate, temperature and species mass fraction is employed at both fuel and oxidizer inlets and their values are presented in Table 1. Supersonic outflow boundary condition is employed for the choked nozzle, i.e. an extrapolated boundary condition is used at the supersonic exit, and the exit pressure is not imposed but followed from the solution. For the chamber wall thermal boundary condition, options of assigning a constant temperature are evaluated, and the temperature of face plate, chamber wall, nozzle wall surfaces are set to measured wall temperature data (754 K, 700 K, 510 K, respectively). All of the injector wall surfaces and oxidizer post tips are assumed to be adiabatic. No-slip conditions are applied at all wall surfaces.

3.3. Initial conditions and calculation procedure

In order to reduce the magnitude of stationary fluctuation inside the combustor, it is important to specify the proper initial condition from which the computations were obtained. The present simulations were accomplished by two procedures. Firstly, steady flow fields were established by using classical, steady RANS method, which ignores unsteady features. Secondly, based on the solutions from steady RANS method the unsteady reaction flow field simulation was accomplished through unsteady DES model. It is noted that combustion flow fields are inherently unstable, which were characterized by a combination of temporal and spatial fluctuations that dominate the mixing and combustion process of non-premixed propellants. The unrealistic predictions obtained from the first classical, steady RANS procedure were just specified as the initial conditions for the second unsteady DES method. Combustion instability was triggered by the transition

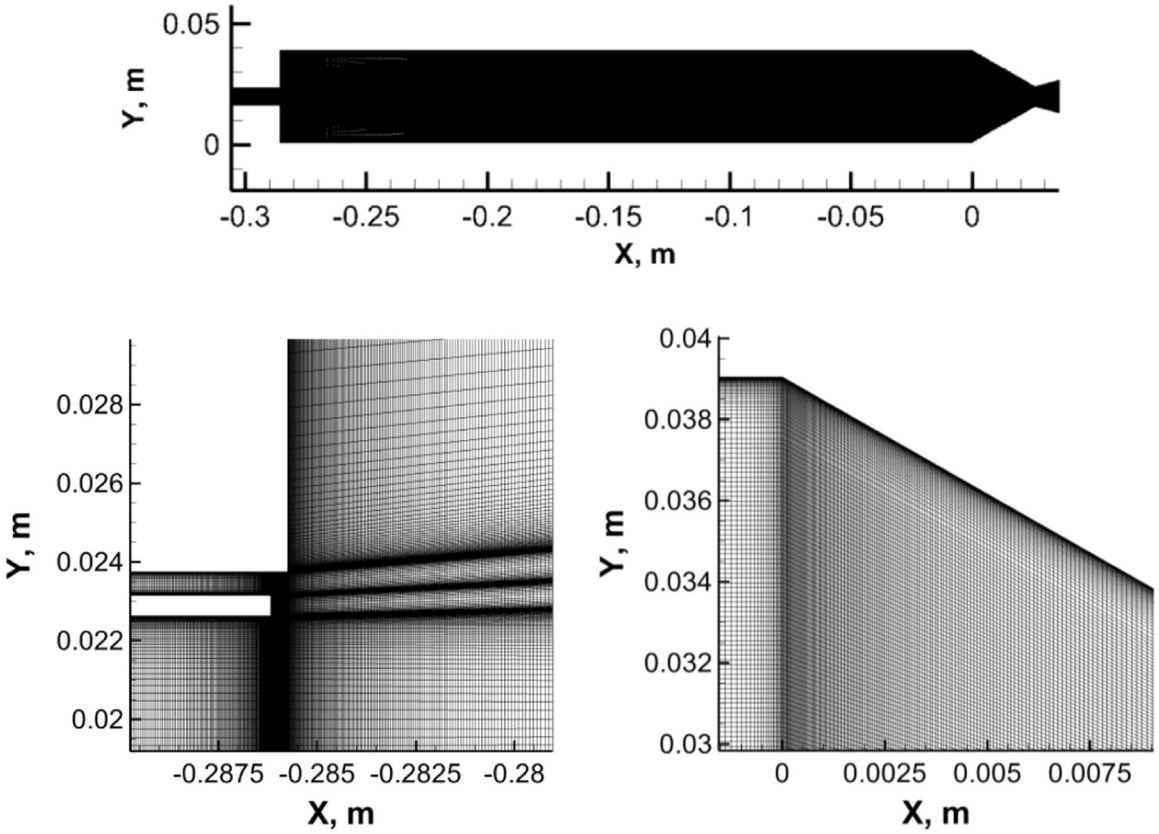

Fig. 3. Details of the computational grid are shown, highlighting the injector (left), and the nozzle (right).

from calculation of RANS to DES and it was similar to the hard ignition. This mechanism of triggering was described and modeled in [21].

4. Validation and precision estimates

Several respective computational techniques have been applied to the common configuration and conditions described in Fig. 1 and Table 1, such as LOGOS code [22], LES using stochastic reconstruction model at Sandia National Laboratories (LES(SNL)), LES with kinetics sub-iteration model at the Georgia Institute of Technology (LES(GIT)), and unsteady RANS at Purdue University (URANS(Purdue)) [23]. Here, Fig. 4 gives the mean wall heat flux predicted by the current simulations and other CFD methods [22,23] along with experiment data. It can be seen that present simulation results are in well agreement to the measurements throughout the entire wall heat flux profile [24,25]. Taking into account the difference of the tools and models, very good agreements between current simulations and other authors' results are obtained. Slight deviations remain close to injector. For details of the difference analysis, the reader can consult reference [23].

As stated in references [22,26], estimating precision and errors accumulation is necessary for large scale simulations of complex combustion gas dynamics in unsteady state flows. Using the same method [22,26], an important characteristic (R_S) for the results of supercomputer simulations is introduced, that is the ratio of maximal allowable number (n_{max}) of time steps to the actual number (n) of time steps used to obtain the results:

$$R_S = \frac{n_{\max}}{n} \tag{5}$$

This ratio, R_S, characterizes reliability of results, i.e. how far below the limit the simulations were finalized, which indirectly characterizes the accumulated error. The higher is the value, R_S, the lower is the error. Here, Table 3 provides data on present simulations, LOGOS code [22] as well as data on LES(GIT) simulations [23]. In contrast to other authors' results, the reliability R_S of present simulations shows a same order of accuracy.

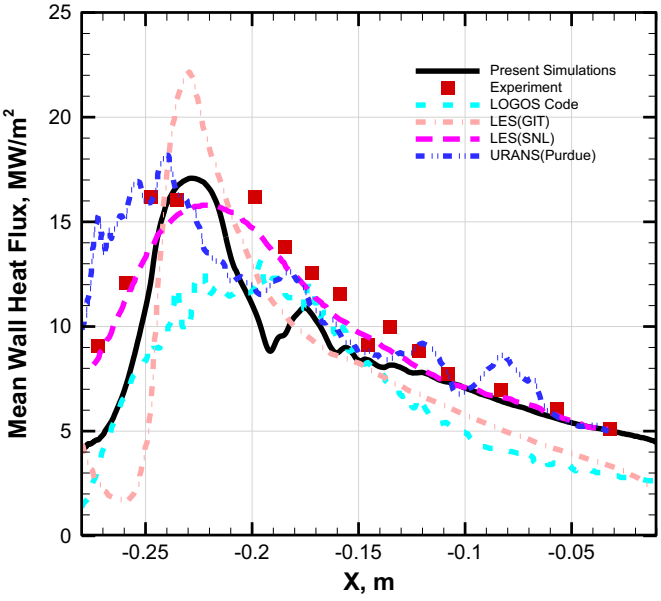

Fig. 4. Heat flux from current simulations, respective calculations as well as corresponding experimental data.

Table 3
Estimates of precision and errors accumulation.

Parameter, dimension	Present simulations	LOGOS code [22]	LES(GIT) [23]
Number of cells	2.5×10^5	9×10^5	3.4×10^6
Number of time steps	8.4×10^5	9×10^6	4×10^6
During of simulations, ms	42	48	41.5
Allowable number of time steps	4.6×10^5	4×10^6	5.7×10^5
Guaranteeing of 10% accuracy reliability, R_S	0.55	0.45	0.14

5. Results and discussion

The results obtained from numerical studies are presented as follows. First, the analytic acoustic resonance frequencies and the corresponding longitudinal modes based on the representative gas properties and combustor geometry are presented. Next, the pressure oscillations are investigated by performing FFT analysis, which gives an indication of how much of the pressure signals coincide with chamber acoustics. Then instantaneous flowfield contours are presented. These contours are useful for understanding combustion instability and give an indication of the low order longitudinal modes. Finally, point probe diagnostics at probe-1 for different fuel-oxidizer velocity ratios are shown, which give an indication of general characteristics and trends, and instantaneous vorticity field of different velocity ratios is shown for comparison.

5.1. Point probe diagnostics and FFT analysis

Point diagnostics are the first type of output, which document the flow variables at selected points in the computational domain. The detailed temporal records enable FFT analysis and filtering to be performed. Although 21 probe points were monitored in the present studies, the results of four locations are shown for brevity. The locations of probes at which pressure signals are recorded are shown in Fig. 5(c). Probe-1 is at the front of the combustor wall, probe-8 is in the middle of the combustor and probe-15 is at the end of the combustion chamber. Acoustic resonance frequencies

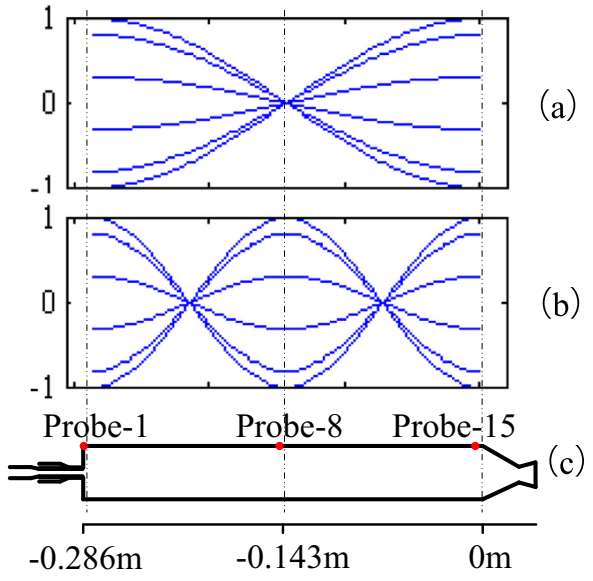

Fig. 5. Spatial mode shapes corresponding to (a) 1st longitudinal mode; (b) 2nd longitudinal mode; (c) schematic of the pressure probes.

Table 4
Analytical frequencies for the acoustic oscillation.

	First order	Second order
Longitude oscillation	2484Hz	4968Hz
Radial oscillation	49.3KHz	98.6KHz

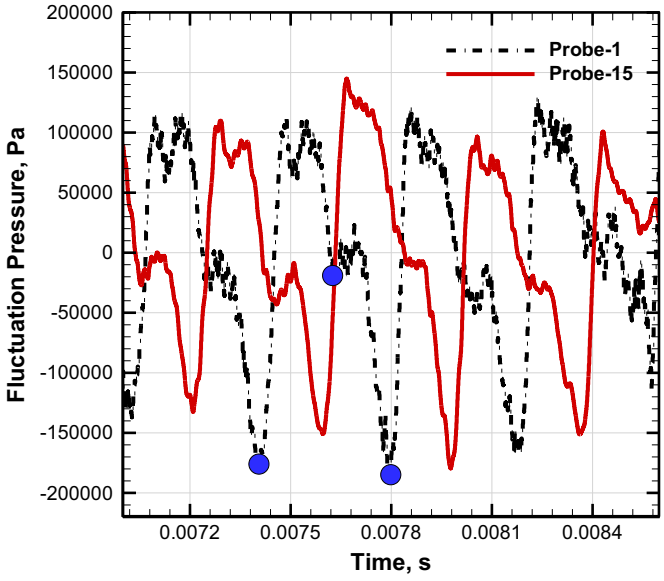

Fig. 6. Time traces of raw pressure at probe-1 and probe-15. Dots on the plot each correspond to a snapshot in Fig. 11.

based on representative gas properties and combustor geometry are shown in Table 4 and the corresponding longitudinal modes are plotted in Fig. 5(a) and (b), a complete description of the method can be found in references [1–3]. As the results shown in Fig. 5, probe-1, 15 locate on the pressure anti-node of longitudinal modes, while probe-8 locates on the pressure node of the first longitudinal mode.

A closer look at the time traces of pressure at probe-1 and probe-15 over a 1.5 ms interval are shown in Fig. 6. As seen from the plots, this interval corresponds to about four dominant oscillation periods. Note that the pressure signals exhibit steep-fronted waves at a dominant frequency that is the characteristic of high amplitude combustion instability. The pressure fluctuations are about 4% of the average chamber pressure.

Also, transient nature of the heat transfer to the wall is highlighted in Fig. 7. It shows the evolution of heat load (integral over the cylindrical part of the chamber) over time and compares the simulated average value with the experimental data, and with the simulated average value from Masquelet et al. [15]. Average heat load of current simulations are shown to agree well with simulation results from reference. Still, slight deviations remain between simulations and experiments. Similar to the results of reference, here, the heat load features a 27% peak-to-peak amplitude.

Fig. 8 displays FFT spectra obtained from the wall pressure signals at different probes, which enables dominant frequencies and oscillation modes to be identified in the combustion chamber. The results used around 30 ms of data providing a frequency resolution of 33 Hz. From this figure, it is seen that probe-1 and probe-15 exhibit very similar trends and results in the data, which identifies frequencies around 2442, 5079, 7619, 10060 Hz. While probe-8 only shows response at 5079, 7619, 10060 Hz. Using Table 4, the 2442 Hz response matches the theoretical 1 L frequency and the waveform graph (shown in Fig. 6) shows probe-1 and probe-15 are out of phase which supports the conclusion that

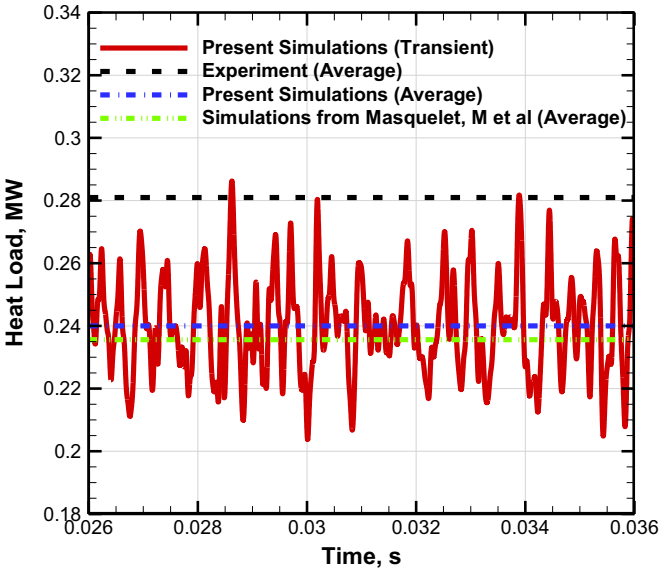

Fig. 7. Evolution of the heat load over time and compares the simulated average with the experimental average, and with the simulated average from Masquelet et al. [15].

longitudinal acoustic responses were excited. Because the location of probe-8 is on the pressure node of the first longitudinal mode (shown in Fig. 5), no response of 2442 Hz is recorded with probe-8, which agrees well with the theoretical analysis. It is interesting to note that Masquelet et al. [15] highlighted the transient nature of the heat transfer to the wall and their results also display a 30% peak-to-peak amplitude as it oscillates at a frequency of around 2.4 kHz.

Fig. 9 displays the FFT spectra of the pressure (probe-1) and vorticity signals. The location of probe at which vorticity signals are obtained is near the exit of annular fuel stream. As seen from the figure, the dominant frequencies in pressure fluctuations match well with the dominant frequencies in vorticity signals. The step height is about 19 mm, if we choose 200 m/s to be the reference velocity which yields a Strouhal number of $(2442 \times 0.019)/200 \approx 0.23$, about the same order of magnitude as what is reported by Cole et al. [27] for a nonreacting axisymmetric jet in a dump combustor. This unsteadiness might be linked to the roll-up frequency of the shear layer.

5.2. *Instantaneous flowfield*

In contrast to the point diagnostics in the combustor, time snapshots of the entire combustion flow field at specific instants of time are useful for deducing the global character of the entire flow-field at a given instant. When these time snapshots are spaced sufficiently closely together in time, they can be converted to flow moves which are helpful for understanding dynamics. Instantaneous snapshots of H_2 mole fraction, temperature and vorticity are shown in Fig. 10. Combined together, these results present the unsteady nature of the combustion flow field. The flame is always anchored at the oxidizer post tips, and the diffusion flames can be observed in the present calculations. The shear layer instabilities due to high speed hydrogen streams lead to large scale vortices being shed downstream. The flame surface exhibits large scale wrinkled structure because of the interaction with the coherent vortices.

Temporal behavior of pressure field in the combustor for a period of the first longitudinal acoustic mode are also shown in Fig. 11, the time interval of each frame is 0.2 ms, dots in Fig. 6 represent the times corresponding to Fig. 11(a)–(c). The pressure

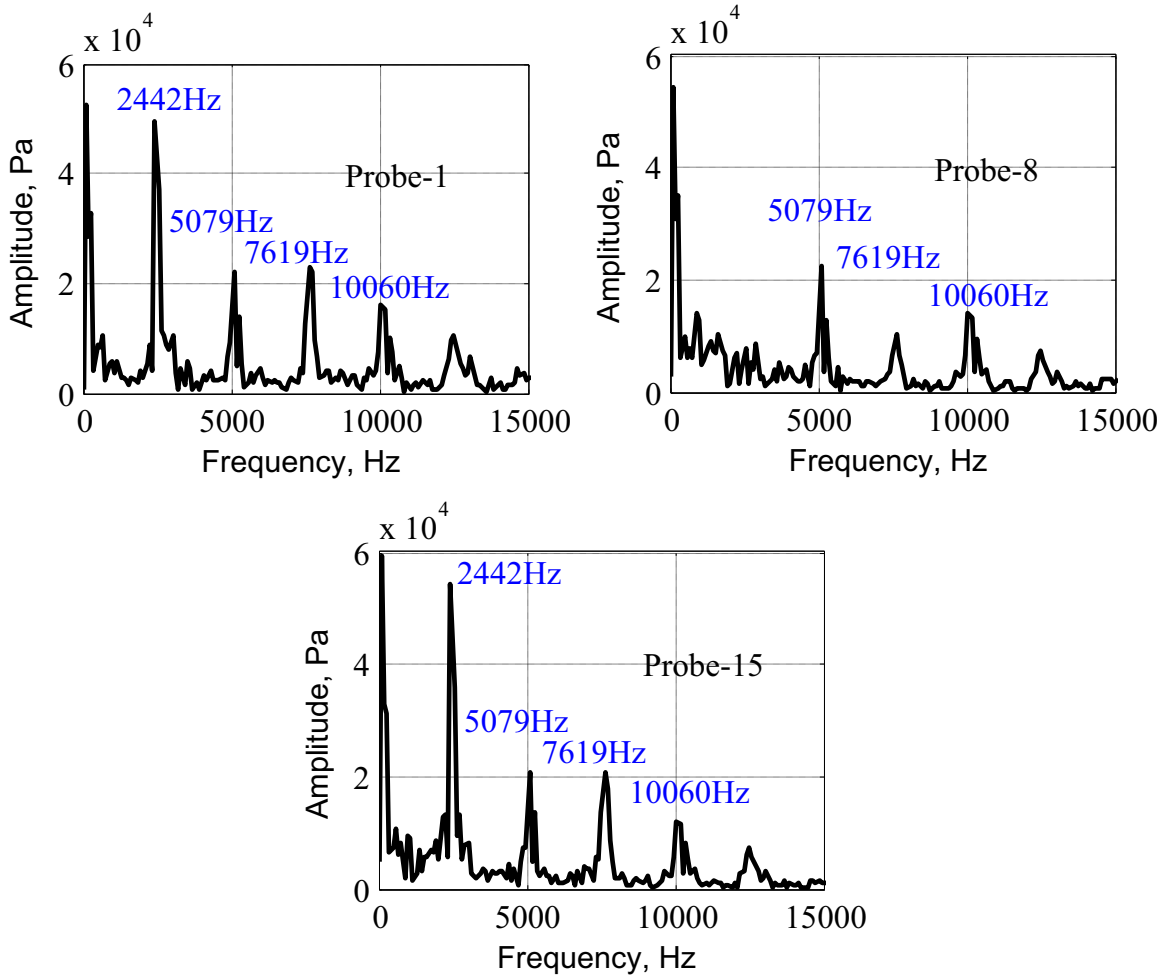

Fig. 8. FFT plots of the pressure signals at different probe points.

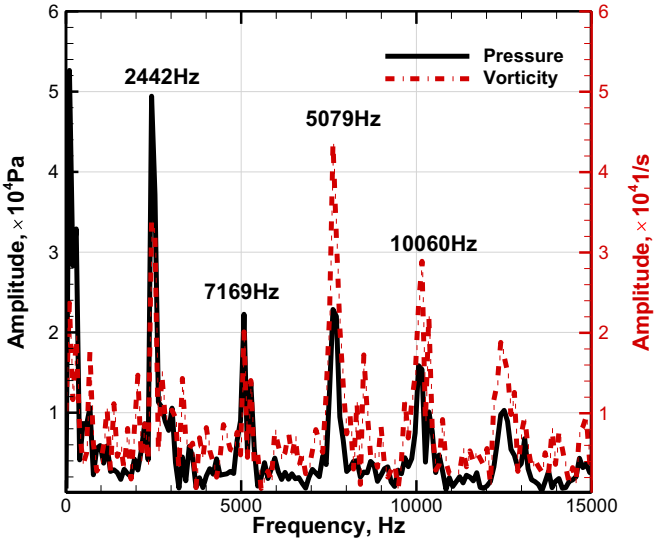

Fig. 9. FFT plots of the pressure and vorticity signals.

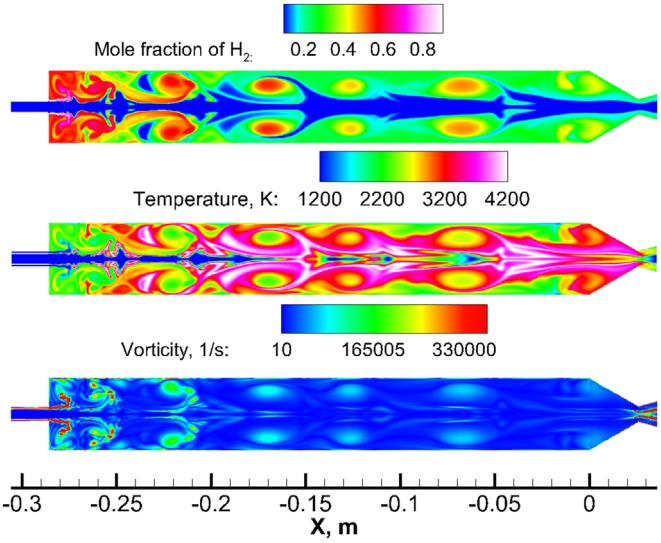

Fig. 10. Instantaneous contours of H_2 mole fraction, temperature and vorticity.

drops due to the vortices and recirculation are observed in the combustor. Remarkable instability is observed in the pressure contours, and the full movie version of these pressure plots shows the pressure wave moving back and forth across the combustor. Half period of single pressure oscillation is about 0.2 ms and its corresponding frequency is about 2.5 kHz. This frequency matches the observed dominant frequency. The patterns of time evolution of pressure field also support that the observed oscillation corresponds to the first longitudinal acoustic mode of combustion chamber.

These flow field snapshots are very valuable in confirming that the flow results obtained from the current calculations are

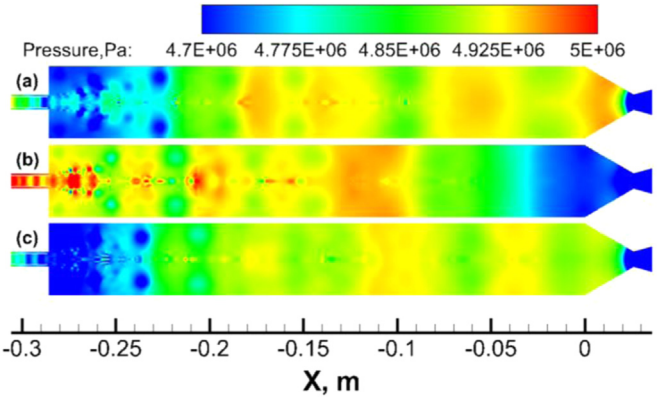

Fig. 11. Temporal behavior of the pressure field with 0.2 ms interval between each frame. The dots on the solid line in Fig. 6 correspond to the times of each snapshot.

reasonable and in understanding the dynamics.

5.3. *Effect of fuel-oxidizer velocity ratio on the combustion instability*

It is classically accepted that combustion instability is sensitive to the operation conditions. Series of numerical simulations were conducted to investigate the effect of fuel-oxidizer velocity ratio on the combustion instability. In the present work, the outer diameter at the outlet of the annular fuel jet is modulated. Thus only the injection velocity of the fuel stream is changed, while other parameters are kept invariant, such as mass flow rate and temperature of the propellant. Three injectors with different velocity ratios are numbered NO. 1, NO. 2, NO. 3, which are summarized in Table 5, and the case of NO. 2 is considered as the baseline, in which the bulk velocity at the outlet of the annular fuel and central oxidizer jet are assumed to be V_1 and V_2 respectively (given in Table 1).

As probe-1 locates on the pressure anti-node of longitudinal modes, the time traces of wall pressure at probe-1 can be used to analyze the effect of velocity ratio on the combustion oscillations. Fig. 12 displays FFT plots corresponding to the frequencies varying from 0 to 15 kHz at probe-1. These FFT results provide an indication of which longitude acoustic modes are being excited and the magnitude of the oscillations at these frequencies. The frequencies obtained from current simulations matches the analytic solutions listed in Table 4. In addition, the low order longitudinal modes (first and second) of the smaller velocity ratio have noticeably larger amplitudes than that of the larger velocity ratio.

Furthermore, low order longitudinal modes and the corresponding oscillation amplitudes of different velocity ratios can be obtained from the band-pass pressure signals. The time history of the band-pass pressure signals filtered from 1300 Hz to 6523 Hz are plotted in Fig. 13. Phase differences (180°) of pressure signals at probe-1 and probe-15 indicate the formation of the fundamental longitude mode. Considering the non-linearity of the waveforms, some discrepancies are legitimate. The resonance modes in the combustor are clearly captured, as anticipated from Fig. 12. It is seen that increase in velocity ratio led to a decrease in the acoustic oscillation amplitude. Note that the larger velocity ratio case has lower peak-to-peak amplitudes than the smaller velocity ratio case but also has fewer portions of higher amplitude. In general, increase in velocity ratio led to a decrease in the acoustic oscillation amplitude.

Table 5
Velocity ratio of the injectors.

Injector number	Velocity ratio (fuel/oxidizer)
NO. 1	$2V_1/3V_2$
NO. 2	$3V_1/3V_2$
NO. 3	$4V_1/3V_2$

To quantify the acoustic-resonance capacity of different velocity ratios, the parameter of acoustic resonance η is investigated, which is calculated by bandwidth method in the form [28]:

$$\eta = \frac{f_2 - f_1}{f_{peak}} \tag{2}$$

Where f_1 and f_2 are the frequencies at which the pressure oscillation amplitude corresponds to $P_{peak}/\sqrt{2}$ with $f_1 < f_2$, and f_{peak} is the frequency at which the peak response (P_{peak}) appears. This equation indicates that bandwidth is broadened as η increases, i.e. the acoustic resonance is weakened.

Fig. 14 shows the FFT spectrum plots of the first longitudinal mode at probe-1 for different velocity ratios ($2V_1/3V_2$, $3V_1/3V_2$ and $4V_1/3V_2$, respectively). When the velocity ratio is set to $2V_1/3V_2$, this gives η equal to 0.038, when the velocity ratio is set to $3V_1/3V_2$, which yields η 0.0573, while when the velocity ratio increases up to $4V_1/3V_2$, eigenfrequency of the system is perturbing around 2500 Hz, the response now covers a broad range of frequencies and features two peaks at 2380 Hz and 2625 Hz with nearly the same amplitude. This calculation indicates that the response bandwidth and amplitude are sensitive to the fuel-oxidizer velocity ratio and a larger velocity ratio acts like a weaker acoustic resonance. Great prominence is put on unraveling the mechanisms.

As shown in Fig. 10, the flame position is affected by the large eddy structures, and this interaction leads to temperature and acoustic velocity based on gas properties perturb, so the eigenfrequency of the system is perturbing around the frequency obtained from the classic acoustic analysis. As expected from the vorticity expression $\left|\nabla\cdot\vec{V}\right|$, when the velocity ratio is augmented, the strength of eddies becomes stronger in the head of the combustion chamber, especially for the large vortical structures further downstream of the combustor demonstrated in the dashed box depicted in Fig. 15, thus temperature and eigenfrequency of the system perturbs more intensively for a larger velocity ratio. It is then natural to inquire whether eigenfrequency fluctuation can reduce the response of the system. Ref. [29] found that response bandwidth is controlled by the level of eigenfrequency fluctuation. The resonance is sharp in the absence of eigenfrequency fluctuation. When the level of eigenfrequency fluctuation is augmented the resonance becomes less pronounced. Therefore eigenfrequency fluctuation serves as a vital source to weak the response and a larger velocity ratio acts like a weaker acoustic resonance. It is interesting to note that the similar phenomenon is retrieved in experiments carried out by Franck et al. [29], though the acoustic resonance is weakened by adding the flame number in their work. In general, in cold jets/wakes which could mimic the flows exiting on a coaxial injectors an increase in velocity ratio can stabilize the flow [30,31]. This could also be related to the trend that increasing velocity ratio provides lower oscillations amplitude.

6. Conclusions and future work

In the present work, results of attempts to capture the self-excited high frequency combustion instability in a rocket combustor are shown. The presence of combustion instability was demonstrated using point measurements, along with FFT analysis and instantaneous flowfield contours. The wall heat flux obtained from calculation shows outstanding agreement with measurement of experiment for the baseline case. The acoustic resonance modes and corresponding frequencies predicted by the present

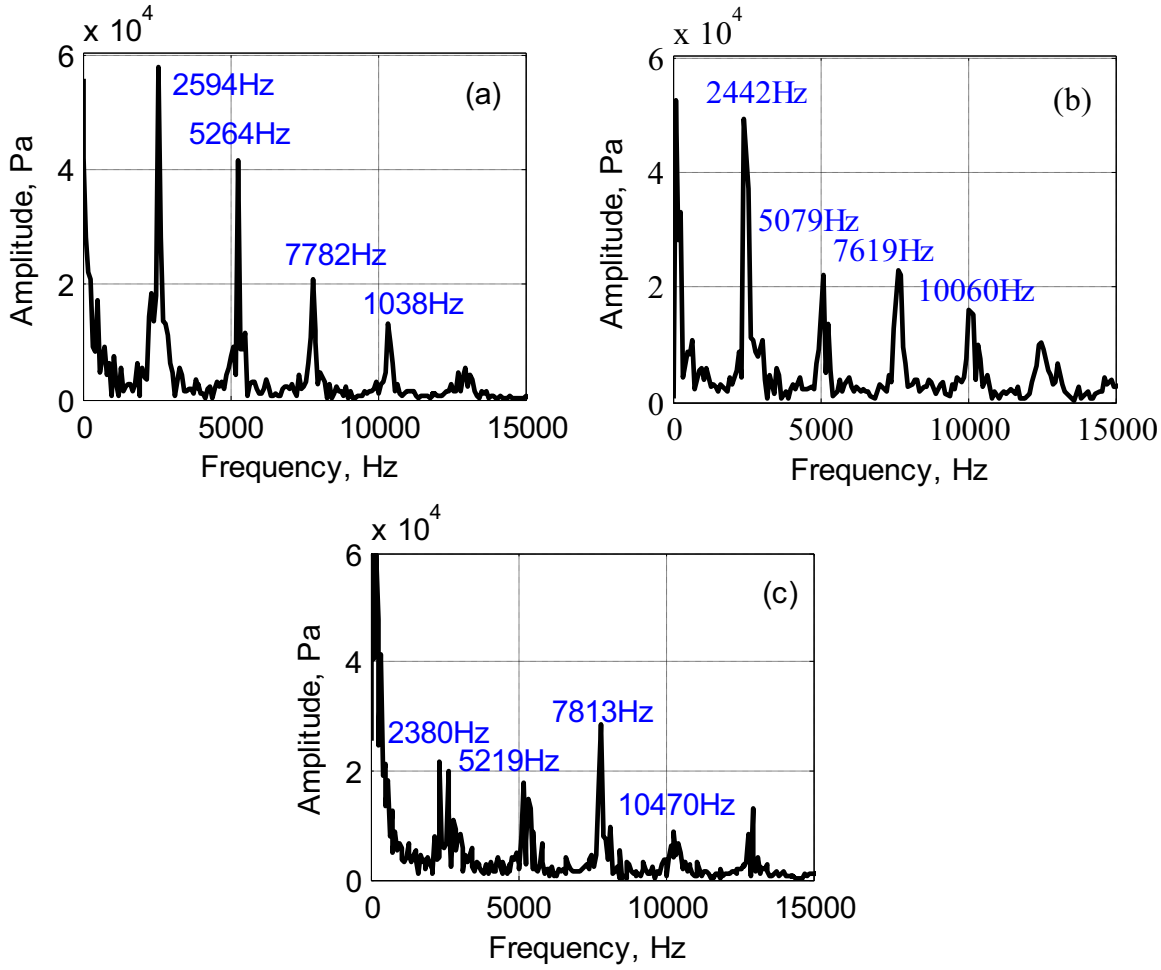

Fig. 12. FFT plots of the pressure signals at probe-1 for different velocity ratios (a) $2V_1/3V_2$; (b) $3V_1/3V_2$; (c) $4V_1/3V_2$.

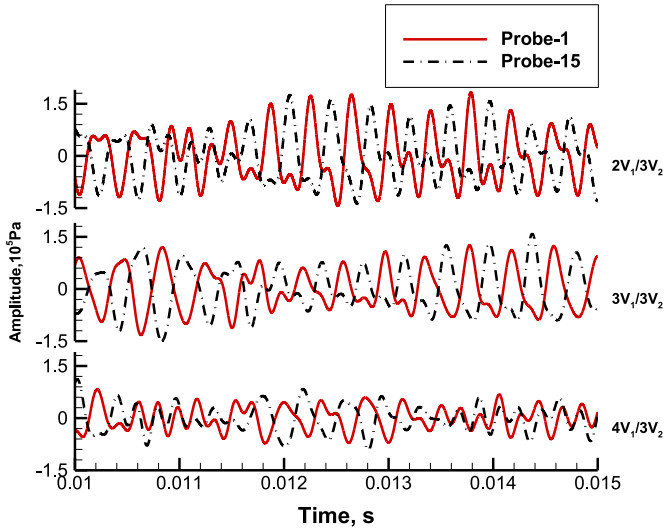

Fig. 13. Time histories of the band-pass pressure oscillations for different velocity ratios.

simulations are almost the same as the results obtained from classic acoustic analysis. Pressure wave moving back and forth across the combustor was also observed.

Then this baseline case was compared against different fuel-oxidizer velocity ratios. Detailed information was obtained from the simulations by comparing FFT plots, band-pass pressure signals and instantaneous flowfield contours. The FFT analysis confirmed the presence of acoustic modes, with significantly higher acoustic pressure oscillations for the smaller fuel-oxidizer velocity ratio than for the larger one. Instantaneous flowfield contours demonstrated that unsteady heat release is linked to the large-scale dynamics. A possible explanation for the trend was given.

Though the current results provided good insight, they are still limited in several ways. The reaction model applied is a simple one-step global reaction, which is likely lead to higher temperatures and more compact heat release models than detailed chemical kinetics. The current calculations are based on the two dimensional simulations, prior simulations have shown the marked advantage of three dimensional simulations over two dimensional models. Further, the present combustion model computes the chemical source terms using Arrhenius expressions, and ignores the effects of turbulent fluctuations. Appropriate turbulent combustion closure may affect the accuracy of the combustion response. The above considerations will form the basis of future investigations.

Acknowledgments

The computations were run on the NUDT supercomputer. The authors would like to thank colleagues from Science and Technology on Scramjet Laboratory for their valuable discussions and comments.

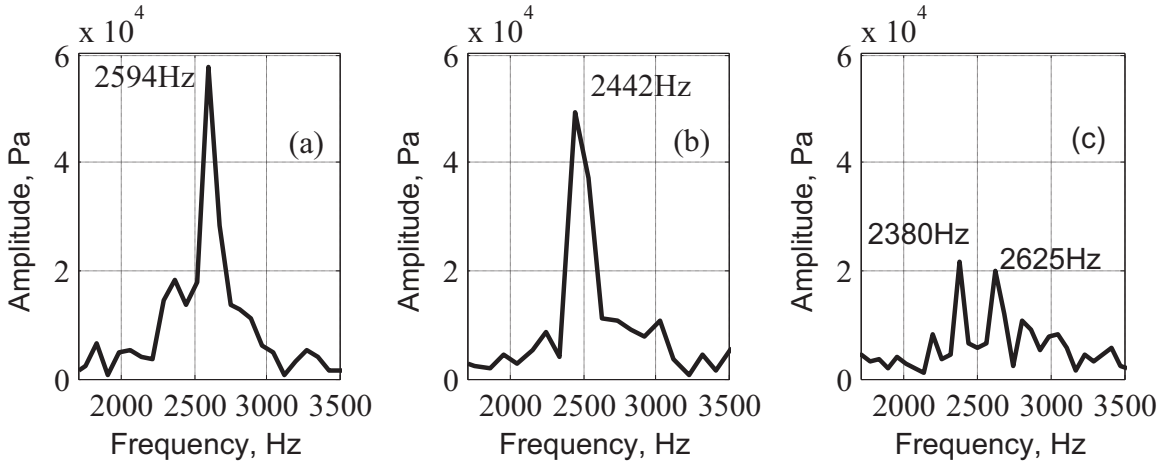

Fig. 14. FFT plots of the 1st longitudinal mode at probe-1 for different velocity ratios (a) $2V_1/3V_2$; (b) $3V_1/3V_2$; (c) $4V_1/3V_2$.

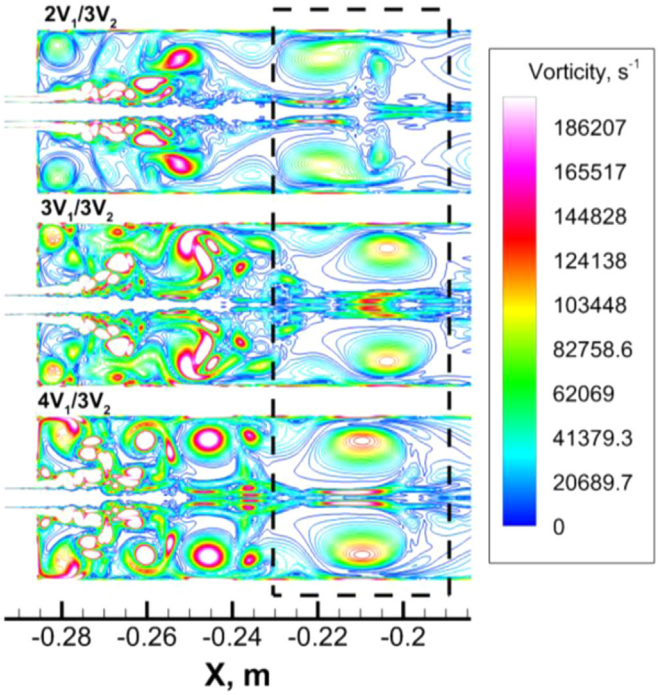

Fig. 15. Vorticity contours for different velocity ratios.

Appendix A. Supplementary material

Supplementary data associated with this article can be found in the online version at http://dx.doi.org/10.1016/j.actaastro.2016.06.015.

References

[1] F.E.C. Culick, Unsteady Motions in Combustion Chambers for Propulsion Systems, AGARD & RTO, Virginia United States 2006, p. 664.
[2] V. Yang, W.E. Anderson, Liquid Rocket Engine Combustion Instability, Washington, 1995.
[3] D.T. Harrje, F.H. Readon, Liquid Propellant Rocket Combustion Instability, NASA, Washington D.C, 1972.
[4] R. Smith, G. Xia, W.E. Anderson, C.L. Merkle, Computational modeling of instabilities in a single-element rocket combustor using a response function, in: Proceedings of the 43rd AIAA/ASME/SAE/ASEE Joint Propulsion Conference & Exhibit, Cincinnati, OH, 2007.
[5] W. Pierre, B. Ramesh, S. Gabriel, M., L.Y. Gicquel, P. Thierry, Using LES to study reacting flows and instabilities in annular combustion chambers, Flow Turbul. Combust. 88 (2012) 191–206.
[6] W. Pierre, S. Gabriel, L.Y.M. Gicquel, J.-D. Müller, P. Thierry, Acoustic and large eddy simulation studies of azimuthal modes in annular combustion chambers, Combust. Flame 159 (2012) 3398–3413.
[7] R. Smith, G. Xia, W.E. Anderson, C.L. Merkle, Extraction of combustion instability mechanisms from detailed computational simulations, in: Proceedings of the 48th AIAA Aerospace Sciences Meeting Including the New Horizons Forum and Aerospace Exposition, Orlando, Florida, 2010.
[8] F. Richecoeur, S. Ducruix, P. Scouflaire, S. Candel, Experimental investigation of high-frequency combustion instabilities in liquid rocket engine, Acta Astronaut. 62 (2008) 18–27.
[9] S. Matsuyama, J. Shinjo, S. Ogawa, Y. Mizobuchi, LES of high-frequency combustion instability in a single element rocket combustor, in: Proceedings of the 50th AIAA Aerospace Sciences Meeting including the New Horizons Forum and Aerospace Exposition, Nashville, Tennessee, 2012.
[10] S. Matsuyama, J. Shinjo, Y. Mizobuchi, LES of high-frequency combustion instability in a rocket combustor, in: Proceedings of the 51st AIAA Aerospace Sciences Meeting including the New Horizons Forum and Aerospace Exposition, AIAA 2013–0564: Grapevine (Dallas/Ft. Worth Region), Texas, 2013.
[11] S. Matsuyama, J. Shinjo, S. Ogawa, Y. Mizobuchi, Large eddy simulation of high-frequency combustion instability of supercritical LOX/GH2 flame, in: Proceedings of the 46th AIAA/ASME/SAE/ASEE Joint Propulsion Conference & Exhibit, Nashville, TN, 2010.
[12] R. Smith, G. Xia, W.E. Anderson, C.L. Merkle, Computational simulations of the effect of chamber diameter on single-element rocket combustor instability, in: Proceedings of the 44th AIAA/ASME/SAE/ASEE Joint Propulsion Conference & Exhibit, Hartford, CT, 2008.
[13] M.E. Harvazinski, W.E. Anderson, C.L. Merkle, Analysis of self-excited combustion instabilities using two- and three-dimensional simulations, J. Propuls. Power 29 (2) (2013) 396–409.
[14] G. Xia, M. Harvazinski, W.E. Anderson, C.L. Merkle, Investigation of modeling and physical parameters on instability prediction in a model rocket combustor, in: Proceedings of the 47th AIAA/ASME/SAE/ASEE Joint Propulsion Conference & Exhibit, San Diego, California, 2011.
[15] M. Masquelet, S. Menon, Large-eddy simulation of flame -turbulence interactions in a shear coaxial injector, J. Propuls. Power 26 (5) (2010) 924–935.
[16] URL: ⟨http://www.fluent.com⟩.
[17] M.E. Harvazinski, Modeling Self-excited Combustion Instabilities Using a Combination of Two- and Three-Dimensional Simulations, Purdue University, West Lafayette, Indiana 2012, p. 240.
[18] M.E. Harvazinski, D.G. Talley, V. Sankaran, Comparison of a structured-LES and an unstructured-DES code for predicting combustion instabilities in a longitudinal mode rocket combustor, in: Proceedings of the 53rd AIAA Aerospace Sciences Meeting, AIAA 2015–1608 Kissimmee, Florida, 2015.
[19] R. Smith, G. Xia, W.E. Anderson, C.L. Merkle, Computational simulations of the effect of backstep height on nonpremixed combustion instability, AIAA J. 48 (9) (2010) 1857–1868.
[20] K.J. Shipley, C. Morgan, W.E. Anderson, Computational and experimental investigation of transverse combustion instabilities, in: Proceedings of the 49th AIAA/ASME/SAE/ASEE Joint Propulsion Conference, AIAA 2013–3992, San Jose, CA, 2013.
[21] N. Noiray, D. Durox, T. Schuller, S. Candel, A unified framework for nonlinear combustion instability analysis based on the flame describing function, J. Fluid Mech. 615 (139) (2008) 139–167.
[22] N.N. Smirnov, V.B. Betelin, R.M. Shagaliev, V.F. Nikitin, I.M. Belyakov, Y. N. Deryuguin, S.V. Aksenov, D.A. Korchazhkin, Hydrogen fuel rocket engines simulation using logos code, Int. J. Hydrog. Energy 39 (2014) 10748–10756.
[23] P.K. Tucker, S. Menon, C.L. Merkle, J.C. Oefelein, V. Yang, Validation of high-fidelity cfd simulations for rocket injector design, in: Proceedings of the 44th AIAA/ASME/SAE/ASEE Joint Propulsion Conference & Exhibit, AIAA 2008–5226: Hartford, CT, 2008.
[24] S. Emre, V. Aravind, S. Corin, S. Wei, Computational assessment of gaseous

reacting flows in single element injector, in: Proceedings of the 47th AIAA Aerospace Sciences Meeting Including The New Horizons Forum and Aerospace Exposition, Orlando, Florida, 2009.
[25] W.M. Marshall, S. Pal, R.D. Woodward, R.J. Santoro, Benchmark wall heat flux data for a GH_2/GO_2 single element combustor, in: Proceedings of the 41st AIAA/ASME/SAE/ASEE Joint Propulsion Conference & Exhibit, Tucson, Arizona, 2005.
[26] N.N. Smirnov, V.B. Betelin, V.F. Nikitin, L.I. Stamov, D.I. Altoukhov, Accumulation of errors in numerical simulations of chemically reacting gas dynamics, Acta Astronaut. 117 (2015) 338–355.
[27] D. Cole, M. Glauser, Applications of stochastic estimation in the axisymmetric sudden expansion, Phys. Fluids 10 (11) (1998) 2941–2949.
[28] I.S. Park, C.H. Sohn, H.J. Kim, Acoustic damping enhanced by gaps in baffled injectors in an acoustic chamber, J. Sound Vib. 330 (2011) 2747–2757.
[29] R. Franck, D. Sébastien, S. Philippe, C. Se´bastien, Effect of temperature fluctuations on high frequency acoustic coupling, Proc. Combust. Inst. 32 (2009) 1663–16710.
[30] M.P. Juniper, The effect of confinement on the stability of two dimensional shear flows, J. Fluid Mech. 565 (2006) 171–195.
[31] L. Biancofiore, F. Gallaire, R. Pasquetti, Influence of confinement on a two dimensional wake, J. Fluid Mech. 688 (2011) 297–320.